Identification of a non-competitive inhibitor of Plasmodium falciparum aspartate transcarbamoylase

Lunev, Sergey; Bosch, Soraya S; Batista, Fernando A; Wang, Chao; Li, Jingyao; Linzke, Marleen; Kruithof, Paul; Chamoun, George; Dömling, Alexander S S; Wrenger, Carsten

Published in:
Biochemical and Biophysical Research Communications

DOI:
10.1016/j.bbrc.2018.02.112

Publication date:
2018

Biochemical and Biophysical Research Communications 497 (2018) 835–842

Contents lists available at ScienceDirect

Biochemical and Biophysical Research Communications

journal homepage: www.elsevier.com/locate/ybbrc

Identification of a non-competitive inhibitor of *Plasmodium falciparum* aspartate transcarbamoylase

Sergey Lunev [a], Soraya S. Bosch [b], Fernando A. Batista [a], Chao Wang [a], Jingyao Li [a], Marleen Linzke [b], Paul Kruithof [a], George Chamoun [a], Alexander S.S. Dömling [a], Carsten Wrenger [b, *], Matthew R. Groves [a, **]

[a] Faculty of Science and Engineering, University of Groningen, Antonius Deusinglaan 1, Groningen, 9713AV, The Netherlands
[b] Unit for Drug Discovery, Department of Parasitology, Institute of Biomedica Sciences, University of São Paulo, Avenida Professor Lineu Prestes 1374, Sao Paulo, SP, 05508-000, Brazil

ARTICLE INFO

Article history:
Received 8 February 2018
Accepted 12 February 2018
Available online 21 February 2018

Keywords:
Malaria
Pyrimidine biosynthesis
Aspartate transcarbamoylase
Inhibitor
2,3-napthalenediol

ABSTRACT

Aspartate transcarbamoylase catalyzes the second step of *de-novo* pyrimidine biosynthesis. As malarial parasites lack pyrimidine salvage machinery and rely on *de-novo* production for growth and proliferation, this pathway is a target for drug discovery. Previously, an apo crystal structure of aspartate transcarbamoylase from *Plasmodium falciparum* (*Pf*ATC) in its T-state has been reported. Here we present crystal structures of *Pf*ATC in the liganded R-state as well as in complex with the novel inhibitor, 2,3-napthalenediol, identified by high-throughput screening. Our data shows that 2,3-napthalediol binds in close proximity to the active site, implying an allosteric mechanism of inhibition. Furthermore, we report biophysical characterization of 2,3-napthalenediol. These data provide a promising starting point for structure based drug design targeting *Pf*ATC and malarial *de-novo* pyrimidine biosynthesis.

1. Introduction

Aspartate transcarbamoylase (EC 2.1.3.2) catalyzes condensation of carbamoyl-phosphate (CP) and L-aspartate to form N-carbamoyl-L-aspartate (CA) and phosphate, the second step in *de-novo* pyrimidine biosynthesis. Unlike humans, malarial parasites lack pyrimidine salvage machinery, making *de-novo* pyrimidine biosynthesis pathway a promising target for drug discovery [1–6].

Crystal structures, as well as inhibitor design have been reported for the fourth, fifth and sixth enzymes of *de-novo* pyrimidine biosynthesis pathway in *P. falciparum*: dihydroorotate dehydrogenase (*Pf*DHODH) [7], orotate phosphoribosyltransferase (*Pf*OPRT) [8] and orotidine 5′-monophosphate decarboxylase (*Pf*OMPDC, PDB: 3N2M). Furthermore, *Pf*DHODH has been validated as a drug target and a number of compounds targeting *Pf*DHODH have entered clinical trials [9]. Dihydroorotase (*Pf*DHO) has been characterized [10], but no crystal structure is available. We recently reported the crystal structure of the unliganded form of *P. falciparum* aspartate transcarbamoylase (*Pf*ATC) [11].

Here we report the identification of a lead compound inhibiting *Pf*ATC (2,3-napthalenediol), a crystal structure of *Pf*ATC with 2,3-napthalenediol as well as biophysical characterization of a subfamily of structurally related compounds. Our crystal structure shows that 2,3-napthalenediol does not bind in the active site of the enzyme and does not significantly affect the binding of the first substrate.

2. Materials and methods

2.1. Expression and purification

Wild type *Pf*ATC-Met3 was cloned, expressed and purified to homogeneity as previously described [11].

2.2. Differential Scanning Fluorimetry (DSF)

Initial screening for *Pf*ATC-Met3 inhibitors was performed against a small molecule library similarly to [11]. Each reaction consisted of 2 μl compound (100 mM stock in 100% DMSO) and 45 μl Master mix (10x Sypro Orange (Invitrogen), 50 μM *Pf*ATC in

* Corresponding author.
** Corresponding author.
E-mail addresses: cwrenger@icb.usp.br (C. Wrenger), m.r.groves@rug.nl (M.R. Groves).

https://doi.org/10.1016/j.bbrc.2018.02.112
0006-291X/

50 mM Tris-HCL pH 8.0 and 300 mM NaCl). Final protein assay concentration was 5 μM, final DMSO concentration was 2% (v/v). Previous assays showed that *Pf*ATC could tolerate up to 10% (v/v) DMSO (data not shown). Control experiments with 2% (v/v) DMSO were performed in each plate. Inflection points of the melting curves were determined using BioRad CSX 96 control software and used as indication of sample thermal stability.

2.3. Microscale Thermophoresis (MST)

MST measurements were performed on a Nanotemper Monolith NT.115 instrument (Nanotemper Technologies GmbH). Purified *Pf*ATC-Met3 was labeled using the RED-NHS Monolith Protein Labelling Kit according to manufacturer's protocol. The labeled protein was concentrated using a centrifugation filter with a 3 kDa cutoff, diluted with glycerol to a final concentration of 50% (v/v) and aliquoted for storage at 193 K. MST measurements were performed in MST buffer (50 mM HEPES pH 8.0, 300 mM NaCl) supplemented with 0.05% (v/v) Tween 20 in standard capillaries (Nanotemper Technologies GmbH). Labeled *Pf*ATC-Met3 was used at a final concentration of 20 nM. The ligands were titrated in 1:1 dilutions following the manufacturer's protocol. All binding reactions were incubated for 10 min followed by centrifugation at 20000*g* prior to loading. All measurements were performed in triplicate at 20–60% LED and 40% MST power.

2.4. Activity measurements

The kinetic properties of *Pf*ATC-Met3 were investigated according to [12] with minor modifications. Enzymatic reactions were performed according to [13] in a total volume of 100 μl in 50 mM Tris-Acetate buffer at pH 8.0; the final concentration of *Pf*ATC-Met3 was 50 nM. Aspartate and carbamoyl-phosphate (CP) saturation curves of the enzyme were assayed using fixed concentrations of CP (2 mM) and aspartate (1 mM), respectively. Small-molecule dose-response curves were measured using assay buffer supplemented with 1% (v/v) DMSO, 2 mM CP and 1 mM aspartate. The reactions were initiated with one of the substrates and quenched after 10 min with 100 μl of Stop mix consisting of two volumes of Antypyrine (26.5 mM 2,3-Dimethyl-1-phenyl-3-pyrazolin-5-one in 50% (v/v) sulphuric acid) and one part of Oxime (80 mM 2,3-Butanedione monoxime in 5% (v/v) acetic acid). After quenching the plates were sealed with transparent sealing tape to prevent evaporation and incubated overnight in the dark at room temperature, according to [12]. After incubation the plates were developed for 30–60 min at 45° in ambient light and the absorbance of the samples was measured at 466 nm using a Synergy H1 Hybrid Reader (BioTek). Positive control experiments with a gradient of carbamoyl-aspartate were performed to provide calibration curves. The carbamoyl-aspartate detection method showed high reproducibility and low or no sensitivity to either substrates or compounds tested. Each reaction was performed in triplicate. Analyses were performed using Microsoft Excel and Graph Pad Prism.

2.5. Crystallization, X-ray data collection and processing

Co-crystallization of *Pf*ATC-Met3 with ligands was performed according to [11] with minor modifications. Namely, the crystallization solution was supplemented with 10 mM of ligand (100 mM stocks in 100% DMSO). Purified product of *Pf*ATC-full expression [11] was screened for crystallization using JCSG *plus* sparse matrix (Molecular Dimensions, Ltd). Diffraction-quality crystal appeared overnight in condition B12 (0.2 M Potassium citrate tribasic monohydrate, 20% (w/v) PEG 3350). All crystals were cryo-protected using crystallization-liquor supplemented with 20% (v/v) glycerol, flash-cooled and stored in liquid nitrogen prior to data collection. Crystallization parameters are summarised in Table 1. Cryo-cooled *Pf*ATC crystals were shipped to the European Synchrotron Radiation Facility (Grenoble). Data collection parameters are summarized in Table 2.

The data collected for *Pf*ATC-Met3 crystals grown in presence of 2,3-napthalenediol were processed using XDSAPP [14] and Aimless [15]. Data for *Pf*ATC-full crystals were automatically collected and processed at the MASSIF-1 beamline [16,17]. The structures were solved and initially refined using the DIMPLE pipeline within CCP4 suite [15] with the coordinates of the unliganded *Pf*ATC-met3 (5ILQ; [11]) as a starting model. The final refinement steps included manual rebuilding in Coot [18] and Refmac5 [19] using locally generated NCS restraints and TLS parameters calculated via the TLSMD web server [20,21].

The resulting crystal structures are deposited in the PDB [22] under accession codes 5ILN (citrate-liganded *Pf*ATC) and 6FBA (2,3-napthalenediol-liganded *Pf*ATC). Data collection and processing statistics are shown in Table 2.

3. Results

As previously reported, full-length *Pf*ATC could not be recombinantly expressed due to spontaneous cleavage of the N-terminal apicoplast targeting sequence [11,23]. Recombinant expression product obtained using a pASK-IBA3-*Pf*ATC-full plasmid encoding full-length *Pf*ATC [11] was used in crystallization trials. This resulted in single *Pf*ATC crystals that diffracted to 2.2 Å at the MASSIF-1 beamline (ESRF). The resulting crystal structure was refined to an R factor and R_{free} of 0.18 and 0.23, respectively.

Analysis of the resulting crystal structure revealed the presence of three *Pf*ATC molecules in the asymmetric unit. Each subunit consisted of 11 α-helixes and 9 β-strands arranged in two folding domains (Fig. 1a and b). The N-terminal carbamoyl-phosphate (CP) binding domain is formed by helixes α1-5 surrounding a flat sheet of β1-4 and α11 piercing through the fold. Similarly, in the C-terminal aspartate-binding domain a central sheet (β5-9) is surrounded by helixes α6-10. Connection of these domains is facilitated through α6 and α11 running in opposite directions. Side chains of α3 and β2 from each subunit form a tunnel in the centre of the trimer. Similar assembly of ATC of other species has been described previously [24] as well as the aspartate transcarbamoylase subunit of human CAD [25].

Oligomeric contacts within the trimer are formed between α4, β1 & β2 of each subunit and α3, α11 and a loop between α11 and β9 from adjacent subunits (Pro333-Val337) (Fig. 1b). Evolutionary conservation of *Pf*ATC and its surfaces has been previously reported [11]. Each of three active sites of the trimer is located in a cavity between N- and C-domains and completed by mobile loop regions α9-β8 (residues 296–313) and α4*-β2* (132–140) from an adjacent subunit (Fig. 1b). For convenience an additional alpha-like region at N-terminus of *Pf*ATC-Cit structure (5ILN) has been labelled as α0. The N-terminus of 5ILN was modelled to Lys30, supporting previously suggested and predicted cleavage site between residues 27–28 (IRT-KK, [11]).

Based on the presence of unambiguous electron density a phosphate and citrate molecules have been modelled within one of the active sites of 5ILN (Fig. 1a and b). Superposition of the N-terminal domains of *Pf*ATC-Cit (5ILN) and apo-structure (5ILQ) revealed a significant shift (3–4 Å) of the entire C-domain towards the N-terminal domain upon citrate binding, resulting in narrower active site (Fig. 1a and b).

Helix α9 as well as the loop between α9 and β8 shaping the C-terminal side of the active site cavity were fully modelled in 5ILN (Fig. 1a and b), while they were omitted from the apo-structure due

Table 1
Table 1 shows crystallization conditions of *Pf*ATC crystal grown in presence of 2,3-napthalenediol as well as the *Pf*ATC-full crystal.

	*Pf*ATC-Met3 with 2,3-Naphthalenediol (6FBA)	*Pf*ATC-Met3-full (5ILN)
Method	Hanging drop	Sitting drop
Plate type	24-well	96-well
Temperature (K)	293	293
Protein concentration (mg ml^{-1})	10	10
Buffer composition of protein solution	20 mM Tris pH 8.0, 300 mM NaCl, 10 mM sodium malonate, 5% (v/v) glycerol, 2 mM BME	20 mM Tris pH 8.0, 300 mM NaCl, 10 mM sodium malonate, 5% (v/v) glycerol, 2 mM BME
Crystallization condition	0.1 M bis-tris propane pH 7.5, 0.2 M Na_2SO_4, 15% (w/v) PEG 3350, 10 mM of 2,3 −Napthalenediol (Final DMSO conc. 10% (v/v))	0.2 M Potassium citrate tribasic monohydrate, 20% (w/v) PEG 3350
Volume and ratio of drop	3 μl (1:1)	2 μl (1:1)
Volume of reservoir	500 μl	50 μl

Table 2
Table. 2 shows data collection, processing and refinement statistics of both structures.
R-factor is defined as $\left(\sum_{hkl}\left|F_{obs}(hkl) - F_{calc}(hkl)\right|\right) \Big/ \sum_{hkl} F_{obs}(hkl)$, where F_{obs} and F_{calc} are observed and calculated structure factors of the reflection of *hkl*, respectively.
R_{merge} is defined as $\sum_{hkl}\sum_{i}\left|I_i(hkl) - < I(hkl) >\right| \Big/ \sum_{hkl}\sum_{i} I_i(hkl)$, where $I_i(hkl)$ is the ith intensity measurement of reflection *hkl* and <I(*hkl*)> is the average intensity from multiple observations.
R_{free} was calculated on the basis of a small subset (5%) of randomly selected reflections omitted from the refinement. Values in parentheses correspond to the highest resolution shell.

	*Pf*ATC-Met3 with 2,3-Naphthalenediol (6FBA)	*Pf*ATC-full (5ILN)
Diffraction source	ID23-1 (ESRF)	MASSIF-1 (ESRF)
Wavelength (Å)	0.979	0.965
Temperature (K)	100	100
Detector	PILATUS 6 M	PILATUS 2 M
Crystal-detector distance (mm)	399.8	323.3
Rotation range per image (°)	0.1	0.15
Number of images	1600	1054
Space group	P 3(2)	P 1 21 1
Cell dimensions		
a, b, c (Å)	86.8, 86.8, 138.2	86.5, 107.3, 87.3
α, β, γ (o)	90.0, 90.0, 120.0	90.0, 117.5, 90.0
Resolution (Å)	43.38–2.05	45.1–2.2
R_{merge}	6.4 (98.1)	10.8 (82.8)
Mean I/σI	11.46 (1.45)	5.0 (0.8)
Completeness (%)	98.7 (98.5)	97.7 (83.8)
CC ½	98.9 (50.6)	98.4 (43.8)
Isa	28.70	36.08
Observed reflections	228939 (37251)	200859 (12804)
Unique reflections	72366 (11695)	69139 (5787)
Redundancy	3.16 (3.18)	2.9 (2.2)
Refinement		
Resolution (Å)	2.0	2.2
No. reflections (unique)	74373	65645
R_{work}/R_{free}	18.4/22.5	17.9/23.4
No. atoms		
Protein	7830	8200
Non-protein	113	52
Water	142	166
Average B-factors		
Protein ($Å^2$)	44.9	51.7
Ligands ($Å^2$)	49.7	60.1
Waters ($Å^2$)	41.1	44.1
R.m.s. deviations		
Bond lengths (Å)	0.025	0.020
Bond angles (°)	2.3	1.97
Ramachandran plot		
Most favored, %	97.3	96.3
Allowed, %	2.5	3.2

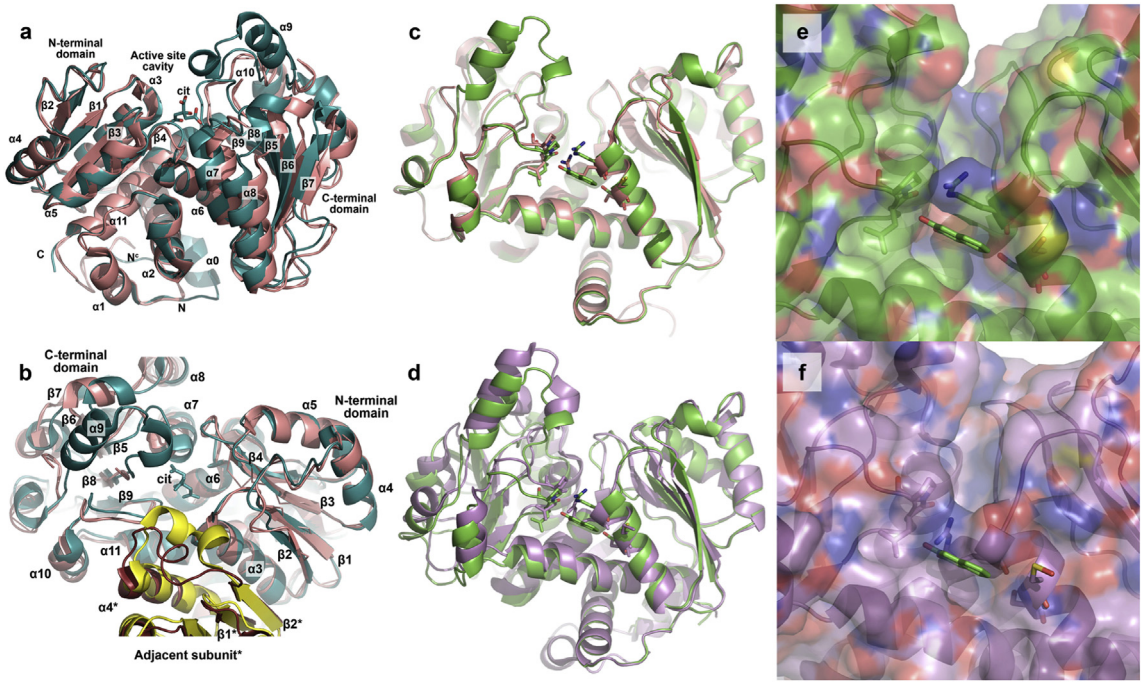

Fig. 1. a & b show unliganded (rose) and citrate-liganded (teal) structures of *Plasmodium falciparum* aspartate transcarbamoylase. Elements of the adjacent subunit are labeled with asterisks (unliganded and citrate-liganded forms are shown in dark red and yellow, respectively). **Fig. 1c & d** show 2,3-napthalenediol liganded structure of *Pf*ATC (green), unliganded (**Fig. 1c**, rose) and citrate-liganded (**Fig. 1d**, purple) *Pf*ATC. **Fig. 1e** shows the surface of the 2,3-napthalenediol binding pocket. The same surface is shown for citrate-liganded (**Fig. 1f**. purple) *Pf*ATC. All figures were generated using PyMol [27]. Superposition of the coordinates of *Pf*ATC structures was performed in Coot [18]. (For interpretation of the references to colour in this figure legend, the reader is referred to the Web version of this article.)

to lack of electron density. This observation suggests stabilization of the active site residues and adjacent regions upon citrate binding. Furthermore, a significant remodelling of the loop between α4 and β3 containing the catalytic Lys138 was observed upon citrate binding (Fig. 1a and b). The entire loop has moved 11.7 Å (Ser133 Cα), bringing Lys138 closer to the active site. These observations suggest that 5ILN with citrate and phosphate bound in the active site can be used as a reasonable model of R-state *Pf*ATC, similarly to the citrate-bound *E. coli* ATC reported by Lipscomb and colleagues [26].

3.1. Hit compound identification

Wild type *Pf*ATC-Met3 was recombinantly expressed and purified as described [11]. Differential Scanning Fluorimetry (DSF) assays performed against a library of small-molecule compounds identified a hit compound (2,3-naphthalenediol, Fig. 2a), significantly increasing the thermal stability of *Pf*ATC-Met3 (ΔT_m 6.5 K, Fig. 2a). Microscale Thermophoresis (MST) assay confirmed binding with dissociation constant (K_d) of 19.9 ± 4.7 μM (Fig. 2b). Further MST analysis showed that at saturating concentrations of 2,3-napthalenediol (100 μM) the affinity of *Pf*ATC to carbamoylphosphate (CP) was not significantly affected. Indeed, *Pf*ATC was shown to bind CP in the presence and absence of 2,3-napthalenediol with dissociation constants of 2.6 ± 0.3 μM and 4.0 ± 0.8 μM, respectively. Similar CP binding was observed for ATC subunit from human CAD (K_d = 6.3 μM) [25]. No binding of aspartate in the absence of CP could be detected in either case.

3.2. 2,3-napthalenediol inhibits PfATC activity

Kinetic measurements performed with *Pf*ATC-Met3 using varying concentrations of substrate allowed identification of optimal assay conditions (Fig. 2c and d). In the presence of 1 mM aspartate wild type *Pf*ATC-Met3 showed sigmoidal cooperative response towards CP (V_{max} = 12.1 ± 0.3 μmol mg^{-1} min^{-1} and Hill slope of 2.7 ± 0.6 (Fig. 2c)). Similarly, in the presence of 2 mM CP, *Pf*ATC-Met3 showed sigmoidal response towards aspartate at concentrations below 1 mM (V_{max} of 10.1 ± 0.4 μmol mg^{-1} min^{-1} and Hill coefficient of 1.5 ± 0.1). At higher aspartate concentrations a strong substrate inhibition effect was observed (Fig. 2d). This correlates with previous observations made for *E. coli* ATC [24] and human ATC CAD subunit [25]. Experiments using 2,3-napthalenediol, performed in 2 mM CP and 1 mM aspartate revealed an IC_{50} value of 5.5 ± 0.9 μM (Fig. 2e), confirming the inhibitory nature of 2,3-napthalenediol.

3.3. 2,3-napthalenediol binds near the active site of PfATC

Crystals of *Pf*ATC-Met3 grown in presence of 10 mM 2,3-naphthalenediol diffracted to a resolution of 2.0 Å (Table 2). The *Pf*ATC-Met3-2,3-naphthalenediol complex crystal structure has been deposited in the Protein Data Bank (PDB) under accession code 6FBA. Analysis revealed three 2,3-naphthalenediol molecules bound in the asymmetric unit (Fig. 3a–c). 2,3-naphthalenediol molecule hydroxyl groups face the Pro333-Pro335 loop opposite Arg109, forming polar contact with the side chain of Glu140 and a water-bridge with Pro333 and Leu334 carbonyl main chain oxygens (Fig. 3c). The naphthalene moiety of 2,3-napthalenediol is located between the α3 helix and the hydrophobic cavity formed by α4 helix and β1-3 sheets of the adjacent subunit.

3.4. Structural re-arrangements associated with 2,3-napthalenediol binding

Binding of 2,3-naphthalenediol did not significantly affect the

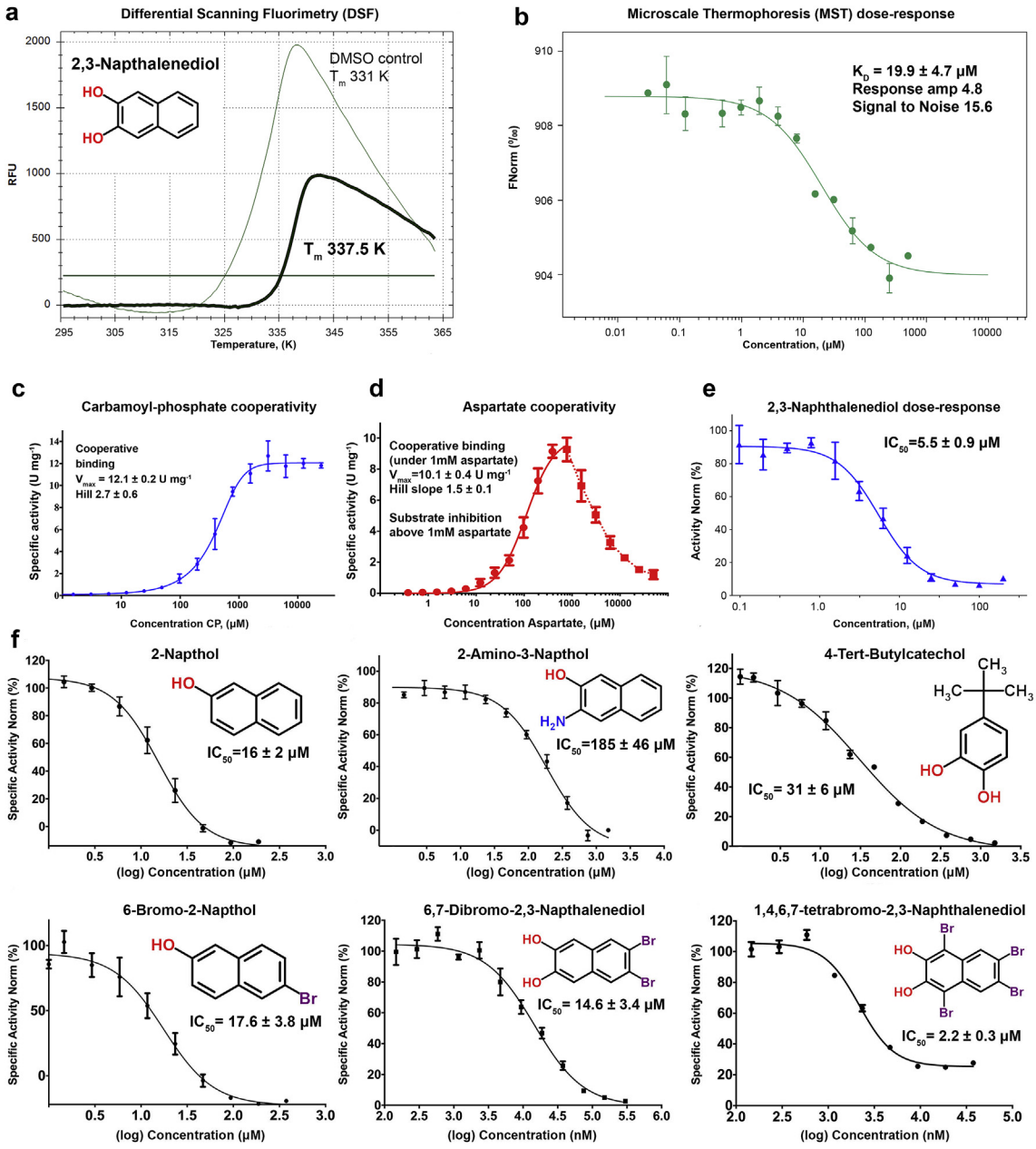

Fig. 2. **a** shows thermal stabilization of *Pf*ATC sample in presence of 2,3-napthalenediol as assessed by DSF. **Fig. 2b** shows binding curve of 2,3-napthalenediol to the fluorescently labelled *Pf*ATC sample as assessed by MST. **Fig. 2c & d** show kinetic parameters of *Pf*ATC as assessed by activity assays. **Fig. 2e** shows inhibition dose-response of *Pf*ATC sample towards increasing concentrations of 2,3-napthalenediol at optimum conditions (**Fig. 2c & d**). **Fig. 2 f** shows inhibitory properties of compounds structurally related to 2,3-napthalenediol. Inhibition dose-response of *Pf*ATC sample towards each compound, compound structures as well as half maximal inhibitory concentrations is shown.

structure of *Pf*ATC compared to the apo-structure (5ILQ, 0.55 Å rmsd on Cα's, Fig. 1c). However, stabilizing effects of 2,3-naphtalenediol, confirmed by DSF experiments (Fig. 1b), were visible in the crystal structure in reduced B-factors for mobile loops α4*-β2*(132–140) and α9-β8 (296–313) of the liganded structure.

Binding of 2,3-naphthalenediol resulted in significant shift in side chain position (4.7 Å between guanidine-groups) of Arg109 as well as Pro333-Pro335 loop shift (1.3 Å towards the compound), while the rest of interacting residues were not significantly affected (Figs. 1c, 4a-c). A shift in Arg109 side-chain position towards the active site resulted in the formation of a channel between the active site cleft and the inter-oligomeric cavity hosting 2,3-naphthalenediol (Fig. 4b, g-i). Slight re-arrangement of the residues forming that cavity resulted in its expansion to accommodate 2,3-naphthalenediol.

Structural comparison with the citrate-bound *Pf*ATC structure (5ILN, N-terminal domain alignment) showed significantly higher position difference of Arg109 main chain (2.8 Å, Fig. 1d) as well as the side chain (4.6 Å between guanidine-groups). Furthermore, the entire C-terminal domain of the citrate-bound *Pf*ATC structure shows significant shift compared to the 2,3-naphtalenediol- and apo-structures (Fig. 1). Positions of the Pro333-Pro335 loops differ by 2.3 Å (Fig. 1d). Significant differences as well as the increased B-factors (5ILN) are observed for the 132–140 loop, compared to the 2,3-naphtalenediol-bound structure (Fig. 4d–f). Movement of the 132–140 loop re-arranges the hydrophobic pocket between α4 helix and β1-3 sheets of the N-terminal *Pf*ATC domain (Fig. 4e–i), making the potential binding of 2,3-naphthalenediol unlikely due

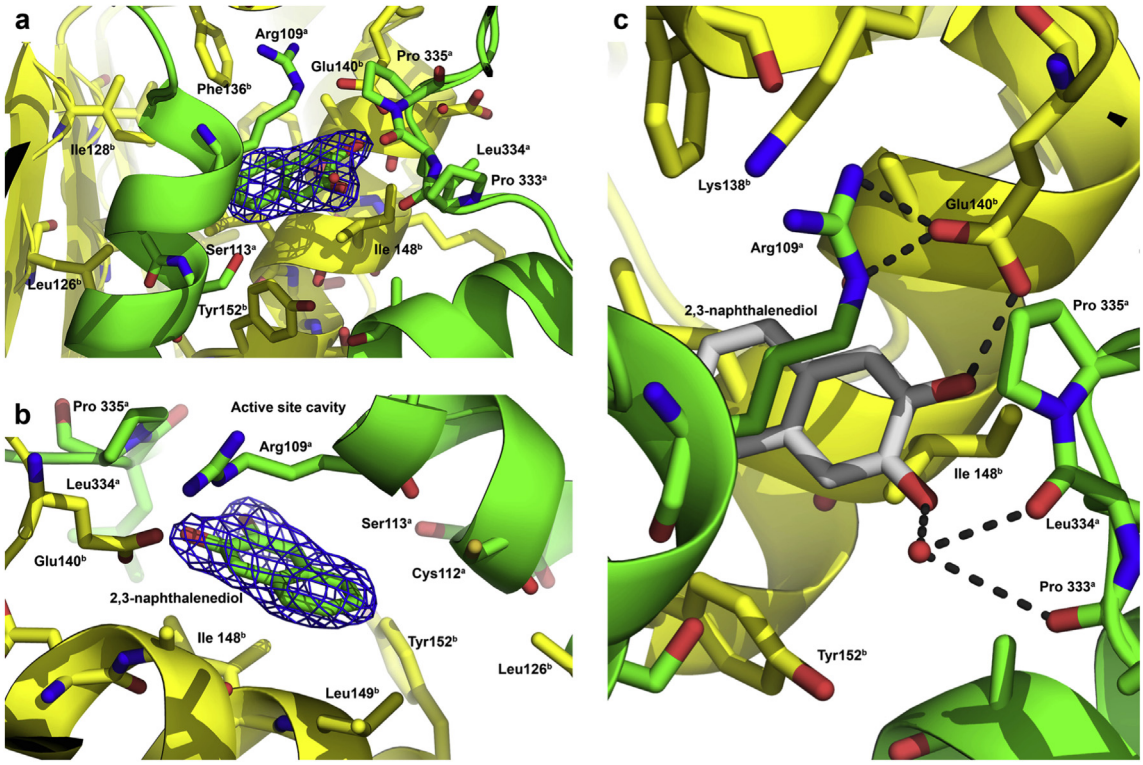

Fig. 3. Fig. 3 shows the binding site of 2,3-napthalenediol between two adjacent subunits labelled as a (green) and b (yellow). Electron density (contoured at 1.2σ) supporting the presence of 2,3-napthalenediol is shown in blue (**Fig. 3a & b**). **Fig. 3c** shows polar contacts between 2,3-napthalenediol and surrounding residues (black dotted lines). (For interpretation of the references to colour in this figure legend, the reader is referred to the Web version of this article.)

to the steric hindrance. Furthermore, the sizes of both the inter-oligomeric cavity and hydrophobic pocket were reduced (Fig. 4i).

3.5. Further compound development

Based on the structure of 2,3-naphthalenediol the inhibitory effects of a sub-family of structurally related compounds were assessed. Dose response of *Pf*ATC towards 2-napthol, 2-amino-3-napthol, 4-*tert*-butylcatechol, 6-bromo-2-napthol, 6,7-dibromo-2,3-napthalenediol and 1,4,6,7-tetrabromo-2,3-napthalenediol was measured (Fig. 2e). None of the tested compounds showed improved inhibition of *Pf*ATC sample with the exception of 1,4,6,7-tetrabromo-2,3-napthalenediol (IC_{50} of 2.2 ± 0.3 μM, Fig. 2e).

4. Discussion

Comparisons of *Pf*ATC complexed with 2,3-napthalenediol, citrate-liganded and un-liganded crystal structures suggest an allosteric mode of inhibition, as 2,3-napthalenediol binds in the cavities formed between adjacent subunits of the trimer (Fig. 3). Significant differences could be observed (Figs. 1d and 4d–f) in comparison with the citrate-bound *Pf*ATC structure (an analogue of the liganded R-state of the enzyme), while no major differences with the apo-structure were detected (Fig. 1c). Furthermore, affinity towards the first substrate CP was not significantly affected by binding of 2,3-napthalenediol and no re-arrangement of the CP-binding mobile loop α4 - β2 (132–140) was detected upon 2,3-napthalenediol binding (Fig. 4a–c). These data imply that 2,3-napthalenediol could "hold" *Pf*ATC in its unliganded-like low affinity T-confirmation. Further optimization of the initial scaffold would likely take advantage of the intersubunit hydrophobic cavity and the induced channel leading to the active site (Fig. 4g–i). Comparison with the ATC subunit of human CAD [25] shows that only eight residues in close proximity of 2,3-napthalenediol are conserved (Arg109, Ser113, Leu126, Glu140, Asp144, Tyr152, Pro333 and Pro335), while the rest of the residues forming the cavity remain diverse. Significantly lower evolutional conservation of 2,3-napthalenediol binding site compared to nearly 100% conserved active site of *Pf*ATC provides an opportunity for selective inhibitor design. Furthermore, the intersubunit cavity of *Pf*ATC hosts a unique pair of cysteines (Cys100, Cys112) from adjacent subunits located approx. 5 Å away from each other. The presence of this cysteine pair is mainly observed in *Plasmodium* species, while none of other ATC's from homologous organisms with sequence identity over 30% possess either Cys 100 or Cys112 (Fig. 2 from Ref. [11]), providing an additional opportunity for highly specific drug discovery targeting *Pf*ATC. Although these two cysteines do not form disulphide bonds in either of the reported structures of *Pf*ATC, their presence is unlikely coincidental, as mutagenic substitution of Cys112 with alanine results in significantly reduced thermal stability of *Pf*ATC (unpublished data). Analysis of the inhibitory properties of compounds structurally related to 2,3-napthalenediol (Fig. 2f) shows that removal or substitution with amino group of one of the hydroxyl groups of 2,3-napthalenediol was not beneficial. Attempts to further exploit the hydrophobic cavity opposite to hydroxy-groups side using brominated 2,3-naptheledіol analogues also did not yield significant improvements.

None of the selected compounds could be clearly observed in co-crystallization trials with the exception of 2-amino-3-napthol and 6,7-dibromo-2,3-napthalenediol. Binding of 2-amino-3-napthol was virtually indistinguishable from 2,3-napthalenediol, however the exact positions of the amino and hydroxyl groups of 2-amino-3-napthol could not be identified. Due to significantly reduced inhibitory properties (Fig. 2f) as well as no detectable

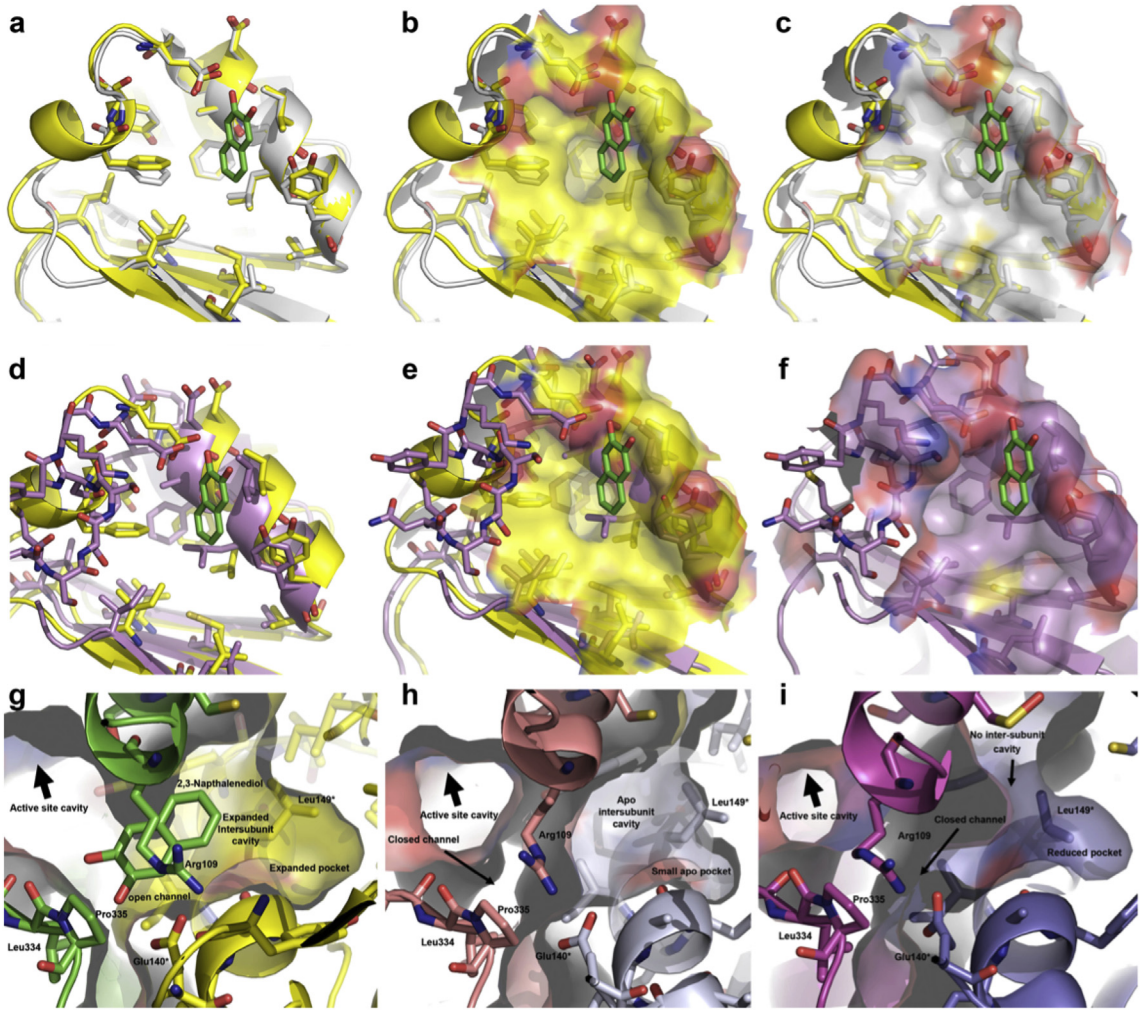

Fig. 4. Fig. 4 shows structural rearrangements of the 2,3-napthalenediol binding site. Comparison of 2,3-napthalenediol-bound (yellow) and unliganded (grey) *Pf*ATC is shown in **Fig. 4a**–**c**, where (a) shows secondary structure comparison, (b) shows the surface of the 2,3-napthalenediol bound structure (yellow), (c) surface of unliganded *Pf*ATC. Similarly, comparison with the citrate-bound structure (purple, 5ILN) is shown in **Fig. 4d**–**f**, where significant re-arrangement can be observed. **Fig. 4g** shows the expanded intersubunit cavity hosting a molecule of 2,3-napthalenediol and a channel connecting this cavity with the active site. Adjacent subunits are shown in green and yellow. In the absence of 2,3-napthalenediol a reduced cavity as well as no channel to the active site can be observed (**Fig. 4h**, rose & grey). In the presence of citrate in the active site (**Fig. 4i**, purple & blue) the intersubunit cavity is significantly remodelled making the binding of 2,3-napthalenediol unlikely due to steric hindrance. (For interpretation of the references to colour in this figure legend, the reader is referred to the Web version of this article.)

thermal stabilization (DSF) and binding to *Pf*ATC (MST) (data not shown), 2-amino-3-napthol was not further addressed in this study. The crystal structure of *Pf*ATC co-crystallized with 6,7-dibromo-2,3-napthalenediol showed the presence of two strong electron density peaks near the binding site of 2,3-napthalenediol, which were interpreted as bromine atoms and further confirmed by anomalous data collected near the bromine absorption edge (data not shown). Due to the lack of unambiguous density allowing the positioning of the naphthalene moiety of the entire compound as well as highly disordered mobile loops α4 - β2 (132–140) and α9 - β8 (296–313), the corresponding structure could not be fully modelled with sufficient confidence and is not reported in this study.

Overall, identification of the inhibiting compound binding in a hydrophobic moderately conserved intersubunit cavity in close proximity of the active site of *Pf*ATC and structural rearrangements associated with it's binding provide an opportunity for further drug developments and could result in highly specific *Pf*ATC inhibitor. Such a compound would aid in validation of *Pf*ATC as a drug target and could be an addition to the antimalarial “toolbox”.

Acknowledgements

The authors would like to acknowledge the ESRF for access and support. We would also like to thank Dr. Christian Kleusch and Dr. Katarzyna Walkiewicz (Nanotemper GmbH) for technical support and advice. This project was supported by the Fundação de Amparo à Pesquisa do Estado de São Paulo grants 2013/17577-9 to SSB, 2014/23330-9 to ML and 2015/26722-8 to CW. Further the authors would like to acknowledge the Ubbo Emmius student fellowships of SSB and ML and the CAPES/Nuffic MALAR-ASP (053/14) network.

Transparency document

Transparency document related to this article can be found online at https://doi.org/10.1016/j.bbrc.2018.02.112.

Appendix A. Supplementary data

Supplementary data related to this article can be found at https://doi.org/10.1016/j.bbrc.2018.02.112.

References

[1] P. Reyes, P.K. Rathod, D.J. Sanchez, et al., Enzymes of purine and pyrimidine metabolism from the human malaria parasite, Plasmodium falciparum, Mol. Biochem. Parasitol. 5 (1982) 275–290.

[2] A.M. Gero, W.J. O'Sullivan, Purines and pyrimidines in malarial parasites, Blood Cell 16 (1990), 467-84; discussion 85–98.

[3] J.E. Hyde, Targeting purine and pyrimidine metabolism in human apicomplexan parasites, Curr. Drug Targets 8 (2007) 31–47.

[4] M.B. Cassera, Y. Zhang, K.Z. Hazleton, V.L. Schramm, Purine and pyrimidine pathways as targets in Plasmodium falciparum, Curr. Top. Med. Chem. 11 (2011) 2103–2115.

[5] S.R. Krungkrai, J. Krungkrai, Insights into the pyrimidine biosynthetic pathway of human malaria parasite Plasmodium falciparum as chemotherapeutic target, Asian Pac J Trop Med 9 (2003) 525–534.

[6] S. Lunev, F.A. Batista, S.S. Bosch, et al., Identification and validation of novel drug targets for the treatment of Plasmodium falciparum malaria: new insights, in: A.J. Rodriguez-Morales (Ed.), Current Topics in Malaria, 2016.

[7] X. Deng, D. Matthews, P.K. Rathod, M.A. Phillips, The X-ray structure of Plasmodium falciparum dihydroorotate dehydrogenase bound to a potent and selective N-phenylbenzamide inhibitor reveals novel binding-site interactions, Acta Crystallogr F Struct Biol Commun 71 (2015) 553–559.

[8] S. Kumar, K. Krishnamoorthy, D.G. Mudeppa, P.K. Rathod, Structure of Plasmodium falciparum orotate phosphoribosyltransferase with autologous inhibitory protein-protein interactions, Acta Crystallogr F Struct Biol Commun 71 (2015) 600–608.

[9] M.A. Phillips, J. Lotharius, et al., A long-duration dihydroorotate dehydrogenase inhibitor (DSM265) for prevention and treatment of malaria, Sci. Transl. Med. 7 (2015) 296 ra111.

[10] S.R. Krungkrai, N. Wutipraditkul, J. Krungkrai, Dihydroorotase of human malarial parasite Plasmodium falciparum differs from host enzyme, Biochem. Biophys. Res. Commun. 366 (2008) 821–826.

[11] S. Lunev, S.S. Bosch, F.A. Batista, et al., Crystal structure of truncated aspartate transcarbamoylase from Plasmodium falciparum, Acta Crystallogr F Struct Biol Commun 72 (2016) 523–533.

[12] L.M. Prescott, M.E. Jones, Modified methods for the determination of carbamyl aspartate, Anal. Biochem. 32 (1969) 408–419.

[13] D.P. Baker, J.M. Aucoin, M.K. Williams, et al., Overexpression and purification of the trimeric aspartate transcarbamoylase from Bacillus subtilis, Protein Expr. Purif. 6 (1995) 679–684.

[14] M. Krug, M.S. Weiss, U. Heinemann, U.X.D.S.A.P.P. Mueller, A graphical user interface for the convenient processing of diffraction data using XDS, J. Appl. Crystallogr. 45 (2012) 568–572.

[15] M.D. Winn, C.C. Ballard, K.D. Cowtan, et al., Overview of the CCP4 suite and current developments, Acta Crystallogr D Biol Crystallogr 67 (2011) 235–242.

[16] M.W. Bowler, D. Nurizzo, R. Barrett, et al., MASSIF-1: a beamline dedicated to the fully automatic characterization and data collection from crystals of biological macromolecules, J. Synchrotron Radiat. 22 (2015) 1540–1547.

[17] O. Svensson, S. Malbet-Monaco, A. Popov, et al., Fully automatic characterization and data collection from crystals of biological macromolecules, Acta Crystallogr. D 71 (2015) 1757–1767.

[18] P. Emsley, B. Lohkamp, W.G. Scott, K. Cowtan, Features and development of Coot, Acta Crystallogr D Biol Crystallogr 66 (2010) 486–501.

[19] G.N. Murshudov, A.A. Vagin, E.J. Dodson, Refinement of macromolecular structures by the maximum-likelihood method, Acta Crystallogr D Biol Crystallogr 53 (1997) 240–255.

[20] J. Painter, E.A. Merritt, Optimal description of a protein structure in terms of multiple groups undergoing TLS motion, Acta Crystallogr D Biol Crystallogr 62 (2006) 439–450.

[21] J. Painter, E.A. Merritt, TLSMD web server for the generation of multi-group TLS models, J. Appl. Crystallogr. 39 (2006) 109–111.

[22] H.M. Berman, J. Westbrook, Z. Feng, et al., The protein data bank, Nucleic Acids Res. 28 (2000) 235–242.

[23] B.J. Foth, S.A. Ralph, C.J. Tonkin, et al., Dissecting apicoplast targeting in the malaria parasite Plasmodium falciparum, Science 299 (2003) 705–708.

[24] W.N. Lipscomb, E.R. Kantrowitz, Structure and mechanisms of Escherichia coli aspartate transcarbamoylase, Acc. Chem. Res. 45 (2012) 444–453.

[25] A. Ruiz-Ramos, A. Velázquez-Campoy, A. Grande-García, et al., Structure and functional characterization of human aspartate transcarbamoylase, the target of the anti-tumoral drug PALA, Structure 24 (2016) 1081–1094.

[26] J. Huang, W.N. Lipscomb, Aspartate transcarbamylase (ATCase) of Escherichia coli: a new crystalline R-state bound to PALA, or to product analogues citrate and phosphate, Biochemistry 43 (2004) 6415–6421.

[27] W.L. DeLano, The PyMOL Molecular Graphics System, DeLano Scientific LLC, Palo Alto, California, USA, 2009. http://www.pymol.org.